

Preparation of Practical High-Performance Electrodes for Acidic and Alkaline Media Water Electrolysis

Gun-hee Moon,^[a, b] Yue Wang,^[a] Seongseop Kim,^[a] Eko Budiyanto,^[a] and Harun Tüysüz^{*[a]}

The synthesis of electrocatalyst and the electrode preparation were merged into a one-step process and proved to be a versatile method to synthesize metal oxide electrocatalysts on the conductive carbon paper (CP). Very simply, the metal precursor deposited on the CP was thermally treated by a torch-gun for just 6 s, resulting in the formation of RuO₂, Co₃O₄, and mixed oxide nanoparticles. The material could be directly used as working electrode for oxygen evolution reaction (OER). Compared with commercial and other state-of-the-art electro-

catalysts, the fabricated electrode showed a superior electrocatalytic activity for OER in 1 M HClO₄ and 1 M KOH in terms of not only a low overpotential to reach 10 mA cm⁻² but also a high current density at 1.6 V_{RHE} with satisfying a long-term stability. The novel strategy without requiring time-consuming and uneconomical steps could be expanded to the preparation of various metal oxides on conductive substrates towards diverse electrocatalytic applications.

Introduction

For several decades, the energy and environmental crisis from fossil fuels has been regarded as one of the most serious issues threatening humanity, and the development of eco-friendly technologies from clean energy sources (e.g., solar-, wind-, hydropower, etc.) can provide the solution to obtain sustainable fuels by preventing the climate change as well as the emission of pollutants.^[1] The electrocatalytic process is the powerful and environmentally benign tool to convert H₂O, CO₂, and N₂ to H₂ gas, (hydro)carbon compounds (i.e., CO and C_xH_yO_z), and ammonia (NH₃), respectively, classified as the most consumed chemical compounds in the world.^[2] From a practical point of view, the electrocatalytic H₂ production is most likely to be feasible since the cleavage of O–H bond is thermodynamically and kinetically favorable compared with that of C=O and N≡N.^[2]

To operate the electrochemical system in an economical way, it is essential to fabricate the electrode with minimizing costs for the manufacture of catalysts and their loading on conductive substrates. In general, most studies carried out in lab-scale experiments follow the standard protocol of (i) the preparation of new catalysts, (ii) the dispersion of catalysts to

make an ink solution, and (iii) the deposition of catalysts onto the conductive substrates [e.g., glassy carbon electrode (GCE), indium-doped tin oxide (ITO) glass, metal foil/foam, etc.] by drop-casting, where Nafion is utilized as a binder. Exceptionally, the one-step process to make the electrode (i.e., a direct synthesis of catalysts onto the conductive substrates) has been limitedly investigated for water electrolysis. For examples, the in-situ generation of cobalt phosphate complex onto the ITO glass is possible by applying anodic bias,^[3] and the chemical spray pyrolysis can make thin film Co₃O₄ and NiCo₂O₄ on CdO-coated glass.^[4] Although a high catalytic activity can be achieved by following the procedure noted above, it is still desirable to develop a fast and cost-effective process for practical and large-scale applications.

The overall water-splitting consists of two parts, hydrogen evolution reaction (HER: 2H⁺ + 2e⁻ → H₂, 0.00 V_{RHE}) and oxygen evolution reaction (OER: 2H₂O → O₂ + 4H⁺ + 4e⁻, 1.23 V_{RHE}), being proceeded at cathode and anode, respectively. While the theoretical potential to cleave water requires 1.23 V_{RHE}, it requires higher potential to overcome the kinetic barrier, where the kinetics of OER with 4e⁻ transfer is more sluggish than that of HER needing 2e⁻ transfer.^[5] Accordingly, to save the total hydrogen production cost it is essential to keep the overpotential on OER as low as possible. Up till now, the development of various types of OER catalysts has been reported in terms of lowering the resistance of intra- and interfacial electron transfer as well as improving the long-term durability against catalyst poisoning and corrosion. For instance, our research has focused on the electrocatalytic water-splitting with preparing well-ordered porous structure using templates or with selective control of hetero-elements incorporation.^[6] Beyond our previous studies, more examples can be given as following: (i) the morphology, crystal phase, porosity, and size (μm to single atom level) control of catalysts,^[7] (ii) the doping, alloying, and solid solution,^[8] and (iii) the hybridization with conductive carbon or other materials.^[9]

[a] Dr. G.-h. Moon, Y. Wang, Dr. S. Kim, E. Budiyanto, Priv.-Doz. Dr. H. Tüysüz
Department of Heterogeneous Catalysis
Max-Planck-Institut für Kohlenforschung
Kaiser-Wilhelm-Platz 1, 45470 Mülheim an der Ruhr (Germany)
E-mail: tueysuez@kofo.mpg.de

[b] Dr. G.-h. Moon
Current address:
Extreme Materials Research Center
Korea Institute of Science and Technology (KIST)
Seoul 02792 (South Korea)

 Supporting information for this article is available on the WWW under <https://doi.org/10.1002/cssc.202102114>

 © 2021 The Authors. ChemSusChem published by Wiley-VCH GmbH. This is an open access article under the terms of the Creative Commons Attribution Non-Commercial License, which permits use, distribution and reproduction in any medium, provided the original work is properly cited and is not used for commercial purposes.

Since the reduction and oxidation reactions proceed in cathode and anode, respectively, electrocatalysts with zero-valent metallic forms or chalcogenide compounds are advantageous for HER, while transition metal (oxy)hydroxides and oxides, which can provide a high-valent oxidation state, are more suitable for OER. In alkaline condition, diverse transition metal oxides and (oxy)hydroxides including Co_3O_4 , CoOOH , Fe_3O_4 , NiO , and $\text{Ni}_x\text{Fe}_{1-x}\text{OOH}$ are frequently used as anode material owing to their high electrocatalytic activities.^[10] On the other hand, most transition metal oxides, in particular metal (oxy)hydroxides, are unstable in acidic media (pH 0–1), and applying anodic bias leads to more severe dissolution.^[11]

Therefore, the design of anode materials is considered more difficult than that of cathode at such a low pH, where the corrosion of metallic catalysts can be retarded via cathodic protection. Amongst various metal oxides, RuO_2 and IrO_2 are known as a relatively durable electrocatalyst at low pH.^[12] Although both Ru and Ir are classified as noble metals, the market price of Ru is roughly 6 times lower than that of Ir (roughly $\$58.9\text{ g}^{-1}$ of Ir vs. $\$9.9\text{ g}^{-1}$ of Ru).^[13] To develop highly efficient and durable ruthenium-based catalysts, the structural modification of RuO_2 has been carried out in terms of the introduction of additional active sites, the change of electronic structure, the increase of a surface area and porosity, and others.^[17] For examples, Kibsgaard et al. synthesized the ordered mesoporous double gyroid RuO_2 using template,^[14] Retuerto et al. tailored sodium-doped SrRuO_3 perovskite,^[15] and Lin et al. reported chromium–ruthenium oxide solid solution for OER.^[16]

In this study, we merged the synthesis of electrocatalysts and the electrode preparation into a one-step process. A simple, super-fast, and eco-friendly method is developed to fabricate the electrodes with a high electrocatalytic activity for water oxidation in 1 M HClO_4 . The RuO_2 nanoparticles, ruthenium molybdenum mixed oxides, as well as Co_3O_4 could be prepared on the conductive carbon paper (CP) by 6 s of heat treatment using a torch-gun. The obtained composite materials could be directly employed as working electrode for OER in acidic and alkaline media. The outcome and activities of the materials go beyond the state of the art of water electrolysis. More promisingly, the developed protocol has a great potential to become a universal method for the synthesis of diverse metal oxides on different types of conductive substrates for various applications.

Results and Discussion

The preparation of RuO_2 has been selected as model system to optimize this practical electrode preparation process. The anode electrode was successfully prepared within a few minutes from handling chemicals to making electrodes. As illustrated in Figure 1a, the CP after drop-casting of the Ru precursor ($\text{RuCl}_3 \cdot x\text{H}_2\text{O}$) solution ($1 \times 1\text{ cm}^2$ geometric area) was thermally treated by using a commercial torch gun for just 6 s under oxygen gas flow (samples are labeled as Ru/CP and T–Ru/CP before and after thermal treatment, respectively). The local

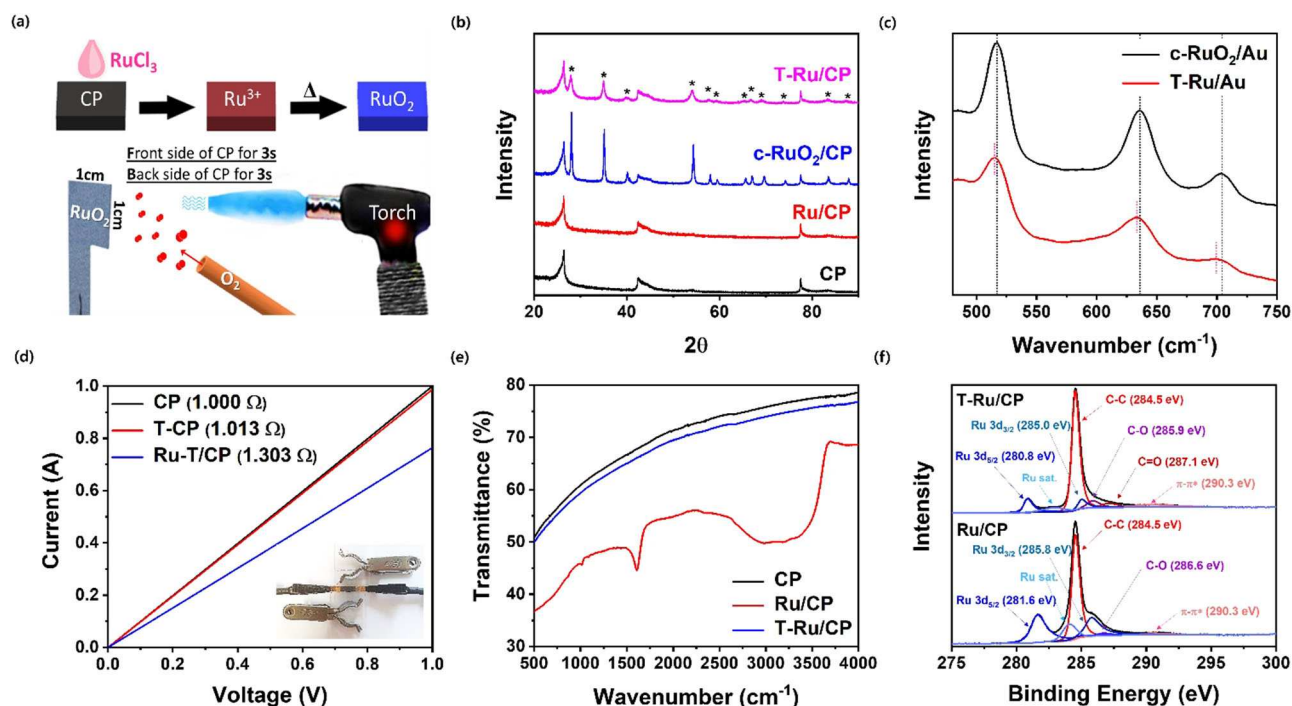


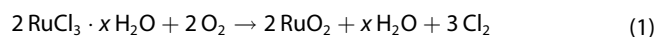
Figure 1. (a) Illustration of preparation of RuO_2 -based electrode. (b) Comparison of XRD patterns for CP, Ru/CP, RuO_2 /CP, and T–Ru/CP. The XRD patterns of RuO_2 were marked by the symbol “*”. (c) Raman spectra of commercial RuO_2 -loaded Au (RuO_2/Au) and thermally treated Ru/Au (T–Ru/Au). To increase the surface enhanced Raman scattering (SERS) effect, the carbon substrate was replaced by gold. (d) Comparison of electrical conductivity of CP, Ru/CP, and T–Ru/CP; the inset shows a picture of the homemade cell. (e) ATR-FTIR spectra of CP, Ru/CP, and T–Ru/CP. (f) High-resolution XPS spectra of C and Ru for Ru/CP and T–Ru/CP.

temperature was controlled by adjusting the distance between the CP and flame of the torch gun (Figure S1). After the thermal shock treatment of 6 s at temperature of around 700 °C (i.e., zone 2), the color of T–Ru/CP was turned into the blue-black. The sponge-like behavior of CP was favorable to absorb ethanol, thus the Ru³⁺ was homogeneously dispersed on the entire of CP (Figure S2). When either the RuCl₃·xH₂O dissolved in water or the polytetrafluoroethylene (PTFE)-treated CP was utilized, the surface of CP remained non-wetting by maintaining the shape of droplet. This indicates that the selection of solvents and substrates is crucial to diffuse metal ions into the carbon substrate.^[18] The advantage of this method is no need for (i) the time-consuming synthetic step of catalysts plus the fabrication of electrodes, (ii) energy-intensive processes such as the calcination at a high temperature for a few hours, (iii) expensive facilities and apparatus, (iv) any stabilizers and templates, and so on. Furthermore, the amount of catalyst loading can be easily controlled via the decrease/increase of either the concentration of precursors or the number of drop-casting time.

In order to investigate the formation of RuO₂ on the CP, the X-ray diffraction (XRD) pattern was collected before and after heat treatment and compared with a commercial RuO₂-loaded CP (c-RuO₂/CP). As shown in Figure 1b, the prominent reflections centered at 26.4, 42.5, and 77.6° in CP are corresponding to (002), (100), and (110) planes of graphite, respectively.^[19] In general, the sp² graphitic carbon is inclined to have a high electrical conductivity, thus it can be utilized as a substrate for electrocatalysis. From 20 to 80°, any peak stemmed from RuCl₃·xH₂O was not observed before thermal treatment, whose observation was similar with XRD pattern of RuCl₃ supported on N-doped graphene reported by Rizescu et. al.^[20] After the thermal treatment, the formation of RuO₂ with rutile phase was observed to be the same as that of commercial RuO₂.^[21] The key difference of T–Ru/CP was the broadening of the peaks, which gives evidence on the formation of much smaller crystallite sizes. The average crystallite size estimated by Scherrer equation [$D = 0.94 \cdot \lambda / \beta \cos(2\theta)$, where $\lambda = 0.154$ nm for Cu K_α radiation of X-ray and β = full width at half maximum (FWHM) at 2θ] was approximately 11 nm. As a rule, the carbon-based materials are not stable against the oxidative decay at high temperature under oxygen atmosphere, but the *d*-spacing calculated at (002) was not changed, and the peak intensity was almost same before and after heat treatment. The heating temperature and time were found to be very critical to synthesize oxide materials. When the heating temperature was too high (zone 3, Figure S1) or the heating time was too long (> 20 s), the formation of metallic Ru was predominant (Figure S3). In reverse, when the heating temperature was too low (zone 1) or the heating time was too short (2 s), the conversion of Ru²⁺ to rigid RuO₂ was not achieved, thus the dissolution of Ru²⁺ into the electrolyte was induced (Figure S4). The average crystallite size of RuO₂ thermally treated for 2, 20, and 40 s in zone 2 was estimated as 6, 25, and 28 nm, respectively, where crystallite size of metallic Ru was calculated to be around 45 nm. Overall, heating of CP-loaded ruthenium precursor for

6 s at the temperature of around 700 °C results in anticipated RuO₂ nanoparticles.

As seen in Figure 1c, Raman spectroscopy of T–Ru/Au also revealed the formation of RuO₂ where three peaks representing E_g, A_{1g}, and B_{2g} modes were seen at 515, 634, and 700 cm⁻¹, respectively. In the case of c-RuO₂/Au, they were observed at 517, 636, and 704 cm⁻¹, correspondingly. Based on the peaks of the bulk single-crystalline RuO₂, typically located at 528, 644, and 716 cm⁻¹, it was confirmed that both T–Ru/Au and c-RuO₂/Au showed a red-shift of the peak position because of either the finite size effect induced by the change of crystalline size or structural stress caused by lattice mismatch.^[22] The larger red-shift in T–Ru/Au relative to c-RuO₂ is the sign for the formation of smaller particles, which matches well with the XRD results. The graphitic carbon materials possess G and D bands, arising from the in-plane optical vibration of aromatic carbon rings and the disorders/defects, respectively. Thus, the degree of the disorder can be inferred by the ratio of D to G band (*I_D/I_G*). As seen in Figure S5, the sharp G band visible in CP, whose *I_D/I_G* was recorded around 0.53, supports good electrical conductivity of the material. The thermal treatment of CP caused the increase of *I_D/I_G*, and the ratio was further increased in case of T–Ru/CP. The rapid thermal shock and the oxidation of graphite can increase the degree of disorder in terms of the introduction of oxygen-containing functional groups (e.g., OH, C=O, C–O, etc.), the distortion of carbon lattice, or the generation of various types of defects, ripples, and edges.^[23] Indeed, the highest value of *I_D/I_G* in T–Ru/CP is possibly ascribed by the interaction between carbon and RuO₂, the decomposition catalyzed by Ru, or the oxidation by Cl₂ evolved as a by-product [Eq. (1)].^[24]



Nevertheless, the intensity of G band was still predominant relative to that of D band, and the peak position of G band was not shifted at all.

The relative comparison of electrical resistance for CP, T-CP, and T–Ru/CP was performed by using a home-made cell (Figure 1d). As the potential was scanned from positive to negative direction, the linear current–potential (*I*–*V*) curves were collected for all samples and the resistance was calculated from the slope of graphs (i.e., $V = IR$). The electrical resistance was almost same before and after heat treatment of pristine CP, while it was risen up to 1.303 Ω for T–Ru/CP. Based on the correlation of Raman spectra with *I*–*V* curves, it can be postulated that the thermal treatment of CP for 6 s could alter the carbon structure (*I_D/I_G* = 0.69) but did not have a profound influence on the change of electrical properties ($R = 1.013 \Omega$). The interaction between highly conductive carbon sheets and RuO₂ nanoparticles with a higher resistivity and possibility of thermal combustion of CP was likely to decline the electrical conductivity in T–Ru/CP.

Attenuated total reflectance Fourier-transform infrared (ATR-FTIR) spectroscopy is a powerful tool to confirm oxygen-containing functional groups, especially in carbon-based compounds and materials. As expected, there was no visible peak in

CP and in commercial RuO_2 powder as well (Figure 1e and S6a). The characteristic Ru–O peak of $\text{RuCl}_3 \cdot x\text{H}_2\text{O}$ at 1585 cm^{-1} was blue-shifted, and the peaks of $\text{RuCl}_3 \cdot x\text{H}_2\text{O}$ observed in entire region except O–H stretch over $2500\text{--}3500\text{ cm}^{-1}$ disappeared in Ru/CP, which might be attributed to the immobilization of Ru^{3+} on carbon or the complexation of Ru^{3+} with ethanol (Figure S6b). Although it was reported that the detection of Ru–Cl stretching is possible at 200 and 300 cm^{-1} , the region is out of range for the commonly used FTIR spectroscopy.^[25]

The heat treatment of Ru/CP completely removed the functional groups of $\text{RuCl}_3 \cdot x\text{H}_2\text{O}$, supporting that the Ru^{3+} was successfully oxidized by the rapid thermal treatment. The change of oxidation states was also confirmed by X-ray photoelectron spectroscopy (XPS). The high-resolution XPS spectra of Ru and C elements for CP, Ru/CP, and T–Ru/CP are shown in Figure 1f and Figure S7. As expected, the majority of C1 s spectrum is attributed to C–C bond, and the peak area of C–O bond is very weak in pristine CP. Among ruthenium species, the binding energies of $\text{Ru } 3d_{5/2}$ for metallic Ru, RuO_2 , RuO_3 , and $\text{RuCl}_3 \cdot 3\text{H}_2\text{O}$ are known as 279.91, 280.68, 282.38, and 282.68 eV, respectively.^[26] The lower binding energy (recorded as 281.6 eV) in Ru/CP implies the interaction between Ru^{3+} and ethanol in terms of a lower electronegativity of oxygen. By the conversion of RuCl_3 to RuO_2 in T–Ru/CP, the $\text{Ru } 3d_{5/2}$ peak was negatively shifted and the peak position (280.8 eV) matches with the reported one. Furthermore, it was confirmed that the rapid heat treatment suppresses the formation of metallic Ru, RuO_3 , or any other ruthenium species. Although the C–O (285.9 eV) and C=O (287.1 eV) groups were introduced after thermal treatment, the intensity is still quite low and the graphitic carbon (284.5 eV) is

relatively well-remained in T–Ru/CP. Based on various spectroscopic data, it can be concluded that Ru^{3+} was successfully oxidized to RuO_2 and the conductive behavior of CP was maintained with 6 s of the heat treatment.

The morphology of T–Ru/CP was confirmed by optical microscope, scanning electron microscope (SEM), and transmission electron microscope (TEM) with a high-resolution (HR) mode. As seen in Figure 2a, the shape of CP resembled a non-aligned mesh woven by carbon thread. This kind of substrate is likely to be advantageous for not only upholding electrocatalysts in comparison to the flat one with a lack of pore and surface roughness but also the mass transfer in electrocatalysis. In bare CP, the surface was clean, and no impurities were observed (Figure S8). With drop-casting of $\text{RuCl}_3 \cdot x\text{H}_2\text{O}$, the wood-like texture of CP disappeared as a result of the surface coating (Figure S9). The energy-dispersive X-ray (EDX) elemental mapping displayed that Ru and Cl were homogeneously dispersed over the entire CP (Figure S10). The heat treatment led to the formation of particles amongst the meshes (Figures 2b and S11a–c) and it was observed that the surface of CP was covered by RuO_2 nanoparticles (Figures 2c and S11d). For TEM measurement, the solution containing CP or T–Ru/CP powder was sonicated and then was loaded on the TEM grid (see Experimental Section in the Supporting Information). As shown in Figure S12, the particulates that came off the CP seemed like agglomerated carbon sheets made of multilayer graphene in that the sonication caused the cleavage of the carbon. The RuO_2 nanoparticles existed in T–Ru/CP (Figure S13), and HRTEM images together with fast Fourier transform (FFT) unveiled that the RuO_2 nanoparticles were aggregated, and the

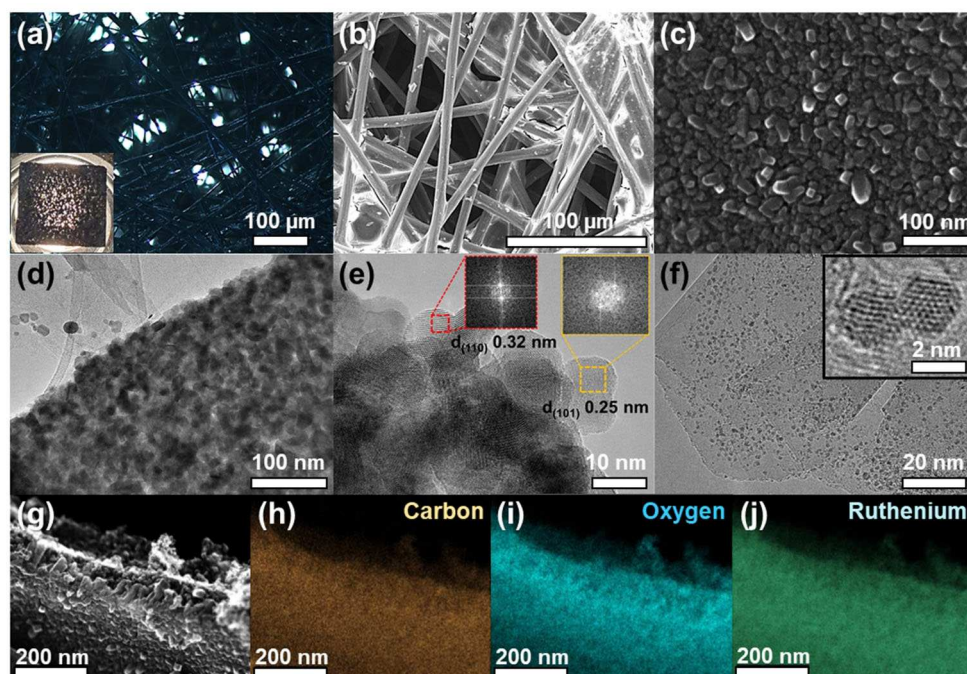


Figure 2. (a) Optical image of T–Ru/CP; the inset is the picture of T–Ru/CP. (b) SEM image of T–Ru/CP. (c) Field-emission (FE)SEM image of the carbon surface in T–Ru/CP. (d–f) TEM and HRTEM images with FFT of T–Ru/CP. (g) STEM image and its EDX elemental mapping of (h) carbon, (i) oxygen, and (j) ruthenium for T–Ru/CP.

lattice space with 0.25 and 0.32 nm corresponded to (101) and (110) face of RuO_2 , respectively (Figure 2e,f).^[21] Furthermore, it was found that nanoparticles with size of around 2 nm were well-dispersed on some part of carbon sheets (Figure 2f), which should be the outer side of carbon thread. Last but not least, scanning TEM (STEM) and its elemental EDX mapping support that Ru and O elements were uniformly distributed over the CP (Figure 2g–j).

After the detailed structural analysis, the prepared composite materials were directly used as a working electrode for OER. The electrocatalytic OER test was carried out in 1 M HClO_4 using a H-type cell separated by Nafion membrane, where the RuO_2 nanoparticles supported on CP was used as anode in a three-electrode system. Figure 3a demonstrates that the time-dependent potential profile fixed at 10 mA cm^{-2} was over $2.0 \text{ V}_{\text{RHE}}$ for pristine CP since there is no active site to initiate 4 e^- transfer. Regarding Ru/CP without heat treatment, the Ru^{3+} was dissolved out when the electrode was immersed into electrolyte, and thus a poor OER activity was observed. The lower potential than that of CP could be attributed to the oxidation of homogenous $\text{Ru}^{\text{II}}(\text{H}_2\text{O})_2^{2+}$ to $\text{Ru}^{\text{VI}}(\text{O})_2^{2+}$ as following Pourbaix diagram.^[27] Although our previous report showed the serial oxidation of Co^{2+} to Co^{4+} under anodic bias contingent upon the generation of $\text{Co}(\text{OH})_2$ in 1 M KOH ,^[28] any anions such as perchlorate, sulfate, nitrate, or others cannot make the complexation with Ru^{2+} in acidic media. Therefore, the calcination to transform metal ions to metals or metal oxides is a

prerequisite for acid water electrolysis. The potential of $\text{c-RuO}_2/\text{CP}$ was reduced down to $1.55 \text{ V}_{\text{RHE}}$ and was unchanged over the time.

The electronic configuration of Ru^{4+} with 4d^4 in RuO_2 , known as one of dn-oxides, can be easily oxidized by the removal of electrons from the partially filled d orbitals, whose chemical activity has higher than that of d^0 -ones. Moreover, the RuO_2 has a high electronic conductivity that is arisen from weak metal–metal bonds, and consequently lies at the apex of Trasatti's volcano plot of metal oxides for OER.^[29] The potential of T–Ru/CP further decreased around $1.44 \text{ V}_{\text{RHE}}$ and remained over the time of the applied potential. In linear sweep voltammetry (LSV) curves, the current density of CP and Ru/CP was identical in the region below $1.6 \text{ V}_{\text{RHE}}$ since the applied bias was not enough to initiate the homogeneous Ru^{3+} -mediated water oxidation (Figure 3b). The current density of T–Ru/CP was 340 mA cm^{-2} at $1.6 \text{ V}_{\text{RHE}}$, which is over six-fold higher than $\text{c-RuO}_2/\text{CP}$ sample that delivered a current density of 54 mA cm^{-2} . This high performance of the T–Ru/CP can be attributed to a few factors including (i) the formation of nanoparticles with more active sites exposed to the electrolyte, (ii) a higher electrochemical surface area and porosity, (iii) a direct electron transfer between carbon and RuO_2 instead of the electron transfer through the interlayer of Nafion binder, and (iv) the utilization of less amount of Nafion that can passivate the surface-active sites of RuO_2 .

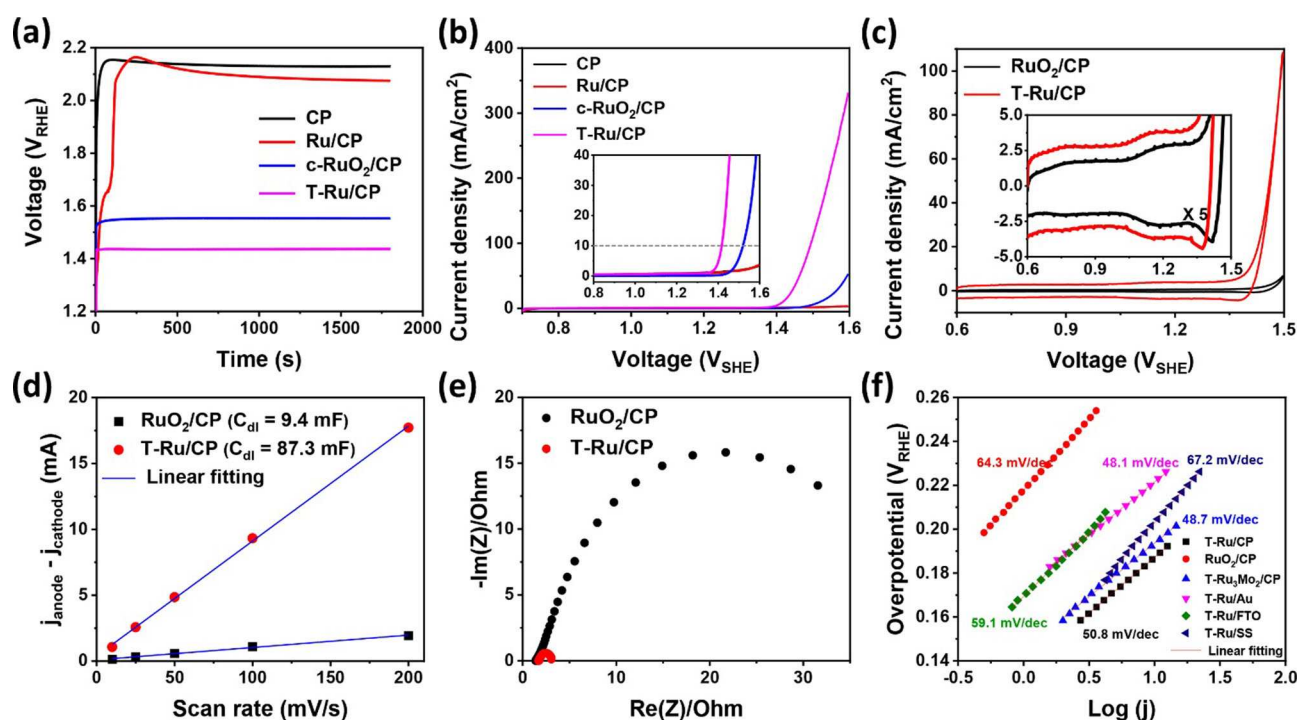


Figure 3. (a) Chronopotentiometry curves fixed at 10 mA cm^{-2} and (b) LSV curves of CP, Ru/CP, $\text{c-RuO}_2/\text{CP}$, and T–Ru/CP. Before collecting chronopotentiometry and LSV, the electrode was stabilized by chronopotentiometry. (c) CV curves of $\text{c-RuO}_2/\text{CP}$ and T–Ru/CP, which are magnified in the inset (the current density of $\text{c-RuO}_2/\text{CP}$ is multiplied by 5). (d) Difference of charging/discharging current densities versus scan rates of RuO_2/CP and T–Ru/CP with linear fitting. (e) Impedance spectroscopy collected at $1.25 \text{ V}_{\text{RHE}}$ of RuO_2/CP and T–Ru/CP. The inset shows the equivalent circuit for modeling OER. (f) Tafel plots for T–Ru/CP, $\text{c-RuO}_2/\text{CP}$, T–Ru/Au, T–Ru/FTO, and T–Ru/SS. Experimental details: H-type cell with Nafion membrane, $10 \mu\text{mol}$ of catalyst on $1 \times 1 \text{ cm}^2$ CP, 1 M HClO_4 , and Ar atmosphere. The potential recorded by Ag/AgCl electrode was converted to reversible hydrogen electrode (RHE).

As seen in Figure 3c, the cyclic voltammetry (CV) curves show that the position of redox potentials in c-RuO₂/CP and T-Ru/CP was almost the same and no new peaks were observed for T-Ru/CP. To investigate correlation of the electrochemical surface area with the catalytic activity, the double layer capacitance (*C_{dl}*) was further calculated from CVs with a different scan rate in a non-faradaic region (Figure 3d). As seen in Figure S14, the rectangular shape of c-RuO₂/CP and T-Ru/CP was maintained with increasing a scan rate. A slight polarization observed in c-RuO₂/CP due to hindering the penetration of electrolytes into the surface of catalysts because of the Nafion binder. The estimated *C_{dl}* of c-RuO₂/CP and T-Ru/CP was 9.4 and 87.3 mF, respectively, which can expound upon the high current density of T-Ru/CP in LSV curves.

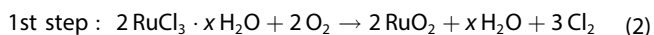
Electrochemical impedance spectroscopy (EIS) was further performed to determine the kinetics of interfacial electron transfer during water electrolysis (Figure 3e). In Nyquist plots, the size of semicircle of T-Ru/CP was much smaller than that of c-RuO₂/CP. The equivalent circuit model developed by Doyle and Lyons was well-fitted (see the inset in Figure 3e) and consequently revealed the resistance affecting the overall kinetics of OER.^[30] *R_Ω*, *R_p*, *R_s*, and *R_{sub}* represent the electrolyte resistance, the polarization resistance, the resistance caused by the formation of intermediates, and the resistance of carbon substrate, respectively. Amongst them, the kinetics of the interfacial charge transfer are governed by *R_p* and *R_s*, whose values were recorded as follows: (*R_p*: 7.031 Ω in RuO₂/CP vs. 0.139 Ω in T-Ru/CP) and (*R_s*: 26.81 Ω in c-RuO₂/CP vs. 0.024 Ω in T-Ru/CP). While *R_p* demonstrates a total charge transfer resistance closely related to the overall OER kinetics, *R_s* stands for the dynamics on the formation of surface intermediates.^[31] Therefore, it can be concluded that not only the interfacial charge transfer to water but also the formation of intermediates was favorable in T-Ru/CP, resulting in the high performance of OER.

To evaluate the feasibility of our protocol for other substrates, the CP was replaced by different types of conductive substrates

including gold plate, fluorine-doped tin oxide (FTO) glass, and stainless-steel (SS) foil. As shown in Figure S15, the RuO₂ was easily detached out from the FTO glass right after applying bias, and the stability of RuO₂ was very poor on the SS foil due to the corrosion. Only the RuO₂ on Au showed a relatively good activity over the time; however, the price of Au is much higher than that of Ru, and thus it is not very practical for real applications.^[13] The CP with a cotton-like morphology is able to provide a higher surface area than that of other substrates with a flat surface, and its sponge-like property can stimulate to absorb the metal precursor solution. Accordingly, the improvement of the electrocatalytic activity is achievable through tailoring morphology as well as the modification of graphitic carbon structure like the doping of hetero-elements into six-membered rings, the control of hydrophobicity/hydrophilicity, the design of well-ordered porous materials with a high surface area, and others.^[32] In order to investigate the kinetics, Tafel plots derived from the overpotential and the logarithmic current density in LSV curves were compared in Figure 3f.^[33]

The Tafel slope can be simply classified into two groups as follows: the low Tafel slope for T-Ru/CP (50.8 mVdec⁻¹) and T-Ru/Au (48.1 mVdec⁻¹) and the high Tafel slope for c-RuO₂/CP (64.3 mVdec⁻¹), T-Ru/FTO (59.1 mVdec⁻¹), and T-Ru/SS (67.2 mVdec⁻¹), which clearly supports that the selection of suitable substrates is important to optimize the OER efficiency.

The stability and durability of electrode material and electrocatalyst should be satisfied for the real application. Stability of the prepared electrodes were further investigated by chronopotentiometry at fixed 10 mAcm⁻² (Figure 4a). The potential in both c-RuO₂/CP and T-Ru/CP was saturated and then kept over 20 h. With a mechanistic point of view, the reaction pathway on the OER over metallic Ru and RuO₂ is very different, and the anodic dissolution is much more severe in metallic Ru. The preparation of metallic Ru on the CP was simply achieved by the modification of the experimental condition that the heat treatment was carried out over 930 °C for 12 s in air [Eqs. (2) and (3)].^[34]



The XRD pattern displays the sharp and broad peaks that are assigned as metallic Ru and RuO₂, respectively, which implies the formation of big metallic Ru particles coexisting with RuO₂ nanoparticles or covered with oxide layers (Figure S16). Based on the Pourbaix diagram, the metallic Ru can be sequentially converted to Ru(OH)₃, RuO₂·2H₂O, and RuO₄ with increasing potential, and the volatile RuO₄ decomposes into RuO₂ and O₂ (Figure S17).^[35] Hence, the overpotential in chronopotentiometry was steadily increased with time (Fig-

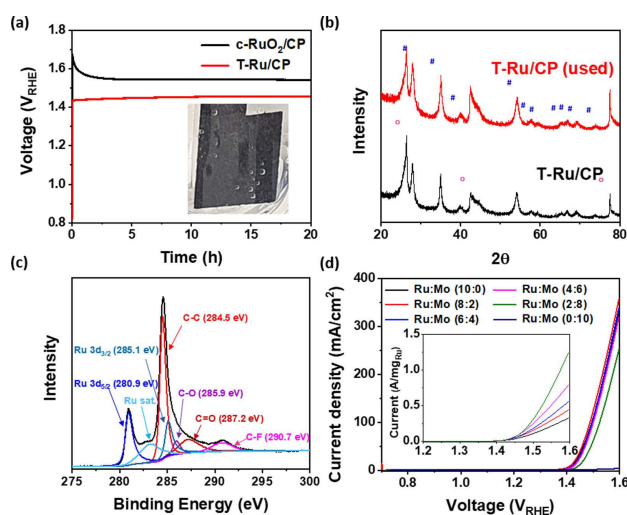


Figure 4. (a) Long-term durability of c-RuO₂/CP and T-Ru/CP. The inset is the photo of T-Ru/CP during the water electrolysis. (b) XRD patterns of T-Ru/CP before and after long-term test. The XRD patterns of RuO₂ and graphitic carbon are marked by the symbol of # and O, respectively. (c) High-resolution XPS spectrum of Ru and C in T-Ru/CP after chronopotentiometry. The C-F peak is observed due to the Nafion. (d) LSV curves of T-Ru_xMo_{3-x}/CP with a different ratio of Ru/Mo. The inset displays the current divided by mass of Ru.

ure S18), and the XRD pattern of metallic Ru disappeared after electrocatalysis (Figure S16).

Moreover, the color of the clamp to hold the electrode was changed from white to black. It has been reported that the electrochemically deposited RuO_2 on the surface of metallic Ru can generate molecular O_2 by direct coupling of O–O present in RuO_2 or from decomposition of RuO_4 as an intermediate.^[36] Indeed, the molecular oxygen also evolved from water oxidation over RuO_2 ^[37] based on peroxide formation mechanism pathway that is predicted by density functional theory (DFT) as shown in Figure S17.^[38] The thermal treatment is an essential prerequisite to retain the durability of RuO_2 in acidic condition.^[39] As a result, the XRD pattern of RuO_2 was not significantly changed before and after chronopotentiometry for 20 h, which was opposite to the case of metallic Ru (Figure 4b). As seen in the XPS spectrum of Ru in T–Ru/CP, implementation of bias for 20 h did not change the binding energy of $\text{Ru}3d_{5/2}$ (Figure 4c). This indicates that RuO_2 is durable under the experimental condition. In spite of many efforts to prevent the corrosion of electrocatalysts, the design of Ru-based electrocatalysts that are completely stable against the dissolution of Ru^{3+} in acidic media has not been reported so far. Although some strategies, such as the surface passivation by Ti ,^[40] the doping of hetero-elements,^[41] the synthesis of mixed oxides,^[42] and others, were proposed, it just delayed the corrosion rate. The dissolution of catalysts is not limited only to acidic conditions, and those issues are also known for alkaline water electrolysis alkaline condition. Overall, our protocol provides the simplest and fastest methodology to synthesize highly active electrocatalysts on conductive substrates in very short time in comparison with the state-of-the-art electrocatalysts that are listed in Table S1.

It has been recently showed that chromium can act as promoter to assist the generation of *OOH species and enhance the performance of ruthenium oxide for OER.^[16] Herein, we explore the possibility of producing mixed electrocatalysts through our versatile methodology by blending ruthenium and molybdenum precursors together. By varying ratios of the precursors, a series of Ru–Mo oxide could be easily prepared (see the Experimental Section for the details). As seen in Figure 4d, the electrocatalytic performance is slightly enhanced when the ratio of Ru to Mo (Ru/Mo, denoted as T- $\text{Ru}_x\text{Mo}_y/\text{CP}$) reached 8:2, and no significant activity change is observed for a ratio of 6:4. For the sample of T- $\text{Ru}_{0.6}\text{Mo}_{0.4}/\text{CP}$, the overpotential fixed at 10 mA cm^{-2} and the Tafel slope are roughly $0.21 \text{ V}_{\text{RHE}}$ and 48.7 mV dec^{-1} , respectively, which are analogous to those of T–Ru/CP (Table S1). Further increasing of Mo up to 2:8 results in decrease of the electrocatalytic performance whereas pristine molybdenum oxide shows negligible OER activity under acidic conditions (Figure 4d and S19). Based on the XRD spectra for T- $\text{Ru}_x\text{Mo}_y/\text{CP}$, the peak intensity of RuO_2 was reduced with increasing Mo content and the related reflections got broader (Figure S20). When the ratio of Ru to Mo was below 6:4, the formation of monoclinic Mo_8O_{23} phase was detected;^[43] its intensity was more visible with the increased amount of Mo. The result indicates that the role of molybdenum oxide was a support to disperse RuO_2 instead of the active site for water

oxidation, and thus the excess amount of Mo in T- $\text{Ru}_x\text{Mo}_y/\text{CP}$ deteriorated the OER performance.

The method is very versatile and can be also applied for the preparation of transition metal oxides like Co_3O_4 -loaded CP ($\text{Co}_3\text{O}_4/\text{CP}$) that can be used for alkaline water electrolysis. As shown in Figure 5a, the formation of nanoparticles could be confirmed by TEM, whose particle size was estimated to be around 10 nm. The HRTEM further confirmed crystallinity of the nanoparticles as seen in the inset of the image. In order to compare the catalytic behavior of $\text{Co}_3\text{O}_4/\text{CP}$, well-defined ordered mesoporous Co_3O_4 was also prepared via nanocasting route by using KIT-6 and SBA-15 silica as hard templates (Figure S21) and deposited on CP. As seen in Figure 5b, XRD patterns indicate presence of crystalline Co_3O_4 spinel besides the graphitic carbon for T- $\text{Co}_3\text{O}_4/\text{CP}$, supporting that the short-time thermal treatment could successfully convert $\text{Co}(\text{NO}_3)_2 \cdot 6\text{H}_2\text{O}$ precursor to Co_3O_4 . The concept resembles the burst nucleation and crystal growth to fabricate typical metal nanoparticles with fine particle size distribution.^[44] Under the experimental conditions (i.e., 1 M KOH, hydrogen reference electrode, and argon atmosphere), the OER performance of T- $\text{Co}_3\text{O}_4/\text{CP}$ was confirmed in terms of the relative comparison with those of ordered mesoporous Co_3O_4 prepared with KIT-6 and SBA-15 silica templates, which are known as very active OER catalysts in alkaline media.^[45,6a] As seen in Figure 5c, the current density of T- $\text{Co}_3\text{O}_4/\text{CP}$ at $1.7 \text{ V}_{\text{RHE}}$ is around 100 mA cm^{-2} , higher than those of mesoporous Co_3O_4 catalysts while the overpotential to reach 10 mA cm^{-2} was much lower for T- $\text{Co}_3\text{O}_4/\text{CP}$.

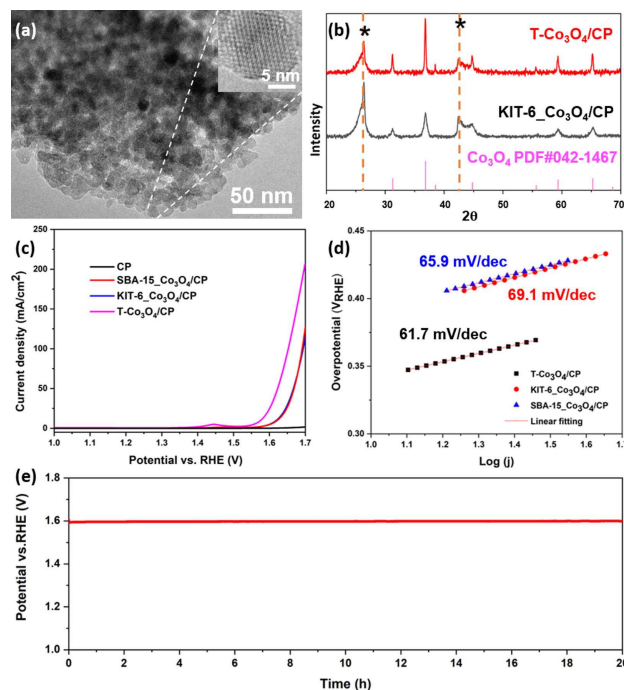


Figure 5. (a) TEM and HRTEM images of T- $\text{Co}_3\text{O}_4/\text{CP}$. (b) Comparison of XRD patterns for T- $\text{Co}_3\text{O}_4/\text{CP}$ and mesoporous KIT-6- $\text{Co}_3\text{O}_4/\text{CP}$. The diffraction peaks CP are marked by the symbol “*”. (c) LSV curves and (d) Tafel plots of T- $\text{Co}_3\text{O}_4/\text{CP}$, mesoporous KIT-6- $\text{Co}_3\text{O}_4/\text{CP}$, and SBA-15- $\text{Co}_3\text{O}_4/\text{CP}$. (e) Long-term durability test of T- $\text{Co}_3\text{O}_4/\text{CP}$ in 1 M KOH.

CP ($0.344 V_{\text{RHE}}$) in comparison with the ordered mesoporous Co_3O_4 ($\approx 0.392 V_{\text{RHE}}$). According to Tafel plots, it was also verified that the electrochemical kinetics on OER for T- $\text{Co}_3\text{O}_4/\text{CP}$ were more favorable than that for ordered mesoporous $\text{Co}_3\text{O}_4/\text{CP}$ (Figure 5d). Similar with the trend in T-Ru/CP, the chronopotentiometry curve displayed that the prepared T- $\text{Co}_3\text{O}_4/\text{CP}$ was stable against the detachment as well as the decomposition of catalysts over 20 h of applied bias (Figure 5e).

Conclusions

We combined the catalyst synthesis and electrode preparation steps into a one-step process. The fabrication of the electrode upholding ruthenium, mixed oxides, and cobalt-based oxide catalysts was successfully achieved via a time-saving and cost-effective innovative protocol. The sponge-like behavior of carbon paper (CP) is favorable to absorb the $\text{RuCl}_3 \cdot x\text{H}_2\text{O}$ and $\text{Co}(\text{NO}_3)_2 \cdot 6\text{H}_2\text{O}$ solution, and the homogeneously dispersed Ru^{3+} and Co^{2+} on the CP could be turned into RuO_2 and Co_3O_4 nanoparticles through thermal treatment by using a torch-gun for just 6 s, respectively. The formed composite material can be directly used as electrode for the oxygen evolution reaction in acidic and alkaline media. The optimized electrocatalysts go beyond the conventional ones prepared by multiple synthetic steps in terms of revealing a low overpotential to reach 10 mA cm^{-2} and delivering a high current density at $1.6 V_{\text{RHE}}$. The electrodes demonstrate excellent stability in both acidic and alkaline media over 20 h of the applied electrical bias. This pioneering method is also expandable to different types of conductive substrates like Au, fluorine-doped tin oxide, and stainless steel, and preparation of binary oxides. The proposed strategy is simple, time-saving, and economical and has a great potential to be applied for the roll-to-roll process for large-scale industrial applications.

Experimental Section

Electrode preparation: Carbon paper (Toray Carbon paper, TGP-H-60, Alfa Aesar) was cut as shown in Figure 1a, and the ink solution containing ruthenium precursor ($\text{RuCl}_3 \cdot x\text{H}_2\text{O}$, Aldrich) was only loaded on the square with $1 \times 1 \text{ cm}^2$. To prepare the ink solution, $\text{RuCl}_3 \cdot x\text{H}_2\text{O}$ was added into ethanol and then vigorously agitated for 30 s for the complete dissolution. $10 \mu\text{L}$ of ink solution was dropcasted onto the front side of carbon paper, which was dried by argon gas flow, and then the same procedure was conducted for the back side (total loading of Ru: $10 \mu\text{mol}$). For thermal treatment, the flame emitted from a commercially available torch was directed to the selected area (i.e., $1 \times 1 \text{ cm}^2$ deposited $\text{RuCl}_3 \cdot x\text{H}_2\text{O}$) under oxygen gas flow for 3 s on the front and back side, respectively. The temperature was recorded to be around 700°C . Before the electrocatalytic test in acidic media, $10 \mu\text{L}$ of Nafion solution [$10 \mu\text{L}$ of Nafion 117 solution (Aldrich) + $990 \mu\text{L}$ of ethanol] was dropped onto the electrode and dried by Ar gas flow. To prepare the mixed oxide consisting of ruthenium and molybdenum, $\text{RuCl}_3 \cdot x\text{H}_2\text{O}$ and molybdenum chloride (MoCl_3 , Alfa Aesar) with a different ratio were mixed in ethanol and sonicated for 30 min to completely dissolve MoCl_3 . As a reference electrode, RuO_2 powder (99.99% trace metals basis, Aldrich) was dissolved in the solution ($980 \mu\text{L}$ of EtOH + $20 \mu\text{L}$

of Nafion solution), and the amount of loading was fixed on the basis of Ru as $10 \mu\text{mol}$. To prepare the metallic ruthenium on CP, the $\text{RuCl}_3 \cdot x\text{H}_2\text{O}$ loaded CP was thermally treated by a lighter in air for 12 s, where the temperature was recorded around 930°C . Similarly, the T-Co/CP electrode was prepared by following the same procedure, whereas the precursor $\text{Co}(\text{NO}_3)_2 \cdot 6\text{H}_2\text{O}$ (Aldrich, 99.999% trace metals basis) was utilized. The mesoporous Co_3O_4 was synthesized by following the protocol noted in Ref. [46].

Characterizations: Transmission XRD patterns were collected by a Stoe theta/theta diffractometer in Bragg-Brentano geometry using $\text{Cu K}_{\alpha 1/2}$ radiation. Raman spectra regarding RuO_2 were obtained using gold substrate to amplify the intensity, and the G and D bands were collected on the CP (Ocean Optics QE Pro-Raman spectrometer using an excitation wavelength of 785 nm). The relative comparison of the resistance for the electrodes was carried out using a homemade cell. The copper tape was utilized as a collector, where the width of copper tape was 4 mm and the gap between two copper tapes attached on the glass holder was 7 mm. To adjust the height as same with copper tape, the side part was covered by scotch tape. The powder sample was loaded on the engraved space, and then it was pressed by another glass holder with two tongs to apply the same pressure. The current-voltage curves were collected by sweeping the potential from 1 to 0 V using a power supply (2450 SourceMeter, KEITHLEY). The functional groups were confirmed by ATR-FTIR spectroscopy (Nicolet Magna 560) using a diamond crystal. XPS analysis was performed with a VG ESCALAB 220i-XL with an X-ray source using monochromatic Al K_{α} anode (1486.6 eV) under the operation at 63 W and 15 kV. SEM and FESEM images with EDX mapping were collected by a Hitachi TM-3030 microscope and a Hitachi S-3500 N electron microscope, respectively. TEM, HRTEM, and STEM images with EDX mapping were taken with a H-7100 electron microscope (Hitachi), a HF-2000 microscope (Hitachi), and a S-5500 microscope (Hitachi), respectively.

Electrochemical activity measurement: Electrochemical data were collected by a three-electrode system: (i) a potentiostat: Biologic SP-150 potentiostat; (ii) a reference electrode: Ag/AgCl (BASi) in 1 M HClO_4 ; (iii) a counter electrode: Pt wire; and (iv) a working electrode: Toray carbon paper, gold plate, FTO glass, or stainless steel loaded with catalysts. The upper part of carbon paper not containing the catalysts was fixed by using a copper clamp covered by Teflon. Not to contact the copper and the carbon paper with electrolyte (*Caution: The clamp made of metal is easily corroded by the contact with 1 M HClO_4 under applying bias.*), the electrode except the region coated by catalysts was pasted by ethylene vinyl acetate, which was melted by a lighter. For acid water electrolysis, the measurement was conducted by using the H-type cell separated by Nafion membrane (Nafion perfluorinated membrane, thickness 0.007 in., Aldrich) under continuous Ar gas purging. The chronopotentiometry measurement was collected as a fixed current at 10 mA and the LSV curves were obtained by sweeping the potential from 0.7 to $1.6 V_{\text{RHE}}$ with a scan rate of 10 mV s^{-1} . Before collecting chronopotentiometry and LSV for c- RuO_2/CP and T-Ru/CP, the electrode was stabilized by chronopotentiometry. CV was performed in the potential range between 0.6 and $1.5 V_{\text{RHE}}$ with a scan rate of 50 mV s^{-1} . In all measurements, the iR drop was compensated at 85% by using the EC-Lab software of BioLogic. For alkaline water electrolysis (1 M KOH), electrochemical data were collected by a three-electrode system: (i) a reference electrode: hydrogen (HydroFlex, Gaskatel); (ii) a counter electrode: Pt wire; and (iii) a working electrode: T-Co/CP electrode.

Acknowledgements

This work was financially supported by the Deutsche Forschungsgemeinschaft (DFG, German Research Foundation) Projektnummer 388390466–TRR 247 within the Collaborative Research Centre/Transregio 247 “Heterogeneous Oxidation Catalysis in the Liquid Phase” and partly by Carbon2Chem consortium funded by the Bundesministerium für Bildung und Forschung (BMBF) of the German government. We thank Max-Planck Society for the support and basic funding. We also sincerely thank N. Pfänder for STEM measurement, S. Palm for FE-SEM measurement, E. Budiyo for HR-TEM and C. Weidenthaler for XPS measurements and related discussions. Open Access funding enabled and organized by Projekt DEAL.

Conflict of Interest

The authors declare no conflict of interest.

Keywords: electrocatalysis · nanoparticles · one-step synthesis · oxides · water oxidation

- [1] V. V. Quaschnig, *Renewable Energy and Climate Change*, 2nd ed., Wiley, 2019.
- [2] Z. W. Seh, J. Kibsgaard, C. F. Dickens, I. Chorkendorff, J. K. Nørskov, T. F. Jaramillo, *Science* **2017**, *355*, eaad4998.
- [3] M. W. Kanan, D. G. Nocera, *Science* **2008**, *321*, 1072–1075.
- [4] R.-N. Singh, M. Hamdani, J.-F. Koenig, G. Poillerat, J. L. Gauttier, P. Chartier, *J. Appl. Electrochem.* **1990**, *20*, 442–446.
- [5] H. Park, H. Kim, G. Moon, W. Choi, *Energy Environ. Sci.* **2016**, *9*, 411–433.
- [6] a) M. Yu, G. Moon, R. G. Castillo, S. DeBeer, C. Weidenthaler, H. Tüysüz, *Angew. Chem. Int. Ed.* **2020**, *59*, 16544–16552; *Angew. Chem.* **2020**, *132*, 16687–16695; b) M. Yu, G. Moon, E. Bill, H. Tüysüz, *ACS Appl. Energ. Mater.* **2019**, *2*, 1199–1209.
- [7] a) M. S. Faber, S. Jin, *Energy Environ. Sci.* **2014**, *7*, 3519–3542; b) C. Zhu, S. Fu, Q. Shi, D. Du, Y. Lin, *Angew. Chem. Int. Ed.* **2017**, *56*, 13944–13960; *Angew. Chem.* **2017**, *129*, 14132–14148.
- [8] a) K. Fominykh, P. Chernev, I. Zaharieva, J. Sicklinger, G. Stefanic, M. Doblinger, A. Muller, A. Pokharel, S. Bocklein, C. Scheu, T. Bein, D. Fattakhova-Rohlfing, *ACS Nano* **2015**, *9*, 5180–5188; b) M. Qian, S. Cui, D. Jiang, L. Zhang, P. Du, *Adv. Mater.* **2017**, *29*, 1704075; c) Y. Hou, S. Cui, Z. Wen, X. Guo, X. Feng, J. Chen, *Small* **2015**, *11*, 5940–5948.
- [9] a) S. Mao, Z. Wen, T. Huang, Y. Hou, J. Chen, *Energy Environ. Sci.* **2014**, *7*, 609–616; b) Y. Yang, K. Zhang, H. Ling, X. Li, H. C. Chan, L. Yang, Q. Gao, *ACS Catal.* **2017**, *7*, 2357–2366.
- [10] a) C. Hu, L. Zhang, J. Gong, *Energy Environ. Sci.* **2019**, *12*, 2620–2645; b) M. Yu, E. Budiyo, H. Tüysüz, *Angew. Chem. Int. Ed.* **2021**, <https://doi.org/10.1002/anie.202103824>.
- [11] X.-K. Gu, J. C. A. Camayang, S. Samira, E. Nikolla, *J. Catal.* **2020**, *388*, 130–140.
- [12] T. Reier, H. N. Nong, D. Teschner, R. Schlögl, P. Strasser, *Adv. Energy Mater.* **2017**, *7*, 1601275.
- [13] Website to check the price of noble metals: www.metalsdaily.com.
- [14] J. Kibsgaard, T. R. Hellstern, S.-J. Choi, B. N. Reinecke, T. F. Jaramillo, *ChemElectroChem* **2017**, *4*, 2480–2485.
- [15] M. Retuerto, L. Pascual, F. Calle-Vallejo, P. Ferrer, D. Gianolio, A. G. Pereira, J. Torrero, M. T. Fernandez-Diaz, P. Bencok, M. A. Pena, J. L. Fierro, S. Rojas, *Nat. Commun.* **2019**, *10*, 2041.
- [16] Y. Lin, Z. Tian, L. Zhang, J. Ma, B. J. Deibert, R. Ge, L. Chen, *Nat. Commun.* **2019**, *10*, 162.
- [17] Y. Yao, L. Lan, X. Li, X. Liu, Y. Ying, J. Ping, *Small* **2020**, *16*, 1907282.
- [18] A. K. Epstein, B. Pokroy, A. Seminara, J. Aizenberg, *Proc. Natl. Acad. Sci. USA* **2011**, *108*, 995–1000.
- [19] Z. Q. Li, C. J. Lu, Z. P. Xia, Y. Zhou, Z. Luo, *Carbon* **2007**, *45*, 1686–1695.
- [20] C. Rizescu, L. Podolean, B. Cojocaru, V. I. Parvulescu, S. M. Coman, J. Albero, H. Garcia, *ChemCatChem* **2017**, *9*, 3314–3321.
- [21] T.-S. Hyun, H. L. Tuller, D.-Y. Youn, H.-G. Kim, I.-D. Kim, *J. Mater. Chem.* **2010**, *20*, 9172–9179.
- [22] S. Y. Mar, C. S. Chen, Y. S. Huang, K. K. Tiong, *Appl. Surf. Sci.* **1995**, *90*, 497–504.
- [23] Y. Zhu, S. Murali, W. Cai, X. Li, J. W. Suk, J. R. Potts, R. S. Ruoff, *Adv. Mater.* **2010**, *22*, 3906–3924.
- [24] A. E. Newkirk, D. W. Mckee, *J. Catal.* **1968**, *11*, 370–377.
- [25] K. Nakamoto, *Infrared and Raman Spectra of Inorganic and Coordination Compounds*, 4th ed., John Wiley & Sons, New York, **1986**.
- [26] C. L. Bianchi, V. Ragaini, M. G. Cattania, *Mater. Chem. Phys.* **1991**, *29*, 297–306.
- [27] A. V. Marenich, A. Majumdar, M. Lenz, C. J. Cramer, D. G. Truhlar, *Angew. Chem. Int. Ed.* **2012**, *51*, 12810–12814; *Angew. Chem.* **2012**, *124*, 12982–12986.
- [28] G. Moon, M. Yu, C. K. Chan, H. Tüysüz, *Angew. Chem. Int. Ed.* **2019**, *131*, 3529–3533.
- [29] S. Trasatti, *Electrochim. Acta* **1984**, *29*, 1503–1512.
- [30] R. L. Doyle, M. E. G. Lyons, *Phys. Chem.* **2013**, *15*, 5224–5237.
- [31] R. L. Doyle, I. J. Godwin, M. P. Brandon, M. E. G. Lyons, *Phys. Chem.* **2013**, *15*, 13737–13783.
- [32] a) G. Moon, A. Bähr, H. Tüysüz, *Chem. Mater.* **2018**, *30*, 3779–3788; b) Y. Zhao, R. Nakamura, K. Kamiya, S. Nakanishi, K. Hashimoto, *Nat. Commun.* **2013**, *4*, 2390; c) X. Song, Y. Chen, M. Rong, Z. Xie, T. Zhao, Y. Wang, X. Chen, O. S. Wolfbeis, *Angew. Chem. Int. Ed.* **2016**, *55*, 3936–3941; *Angew. Chem.* **2016**, *128*, 4004–4009.
- [33] L. Negahdar, F. Zeng, S. Palkovits, C. Broicher, R. Palkovits, *ChemElectroChem* **2019**, *6*, 5588–5595.
- [34] J. A. Rard, *Chem. Rev.* **1985**, *85*, 1–39.
- [35] Y. Sugawara, A. P. Yadav, A. Nishikata, T. Tsuru, *J. Electrochem. Soc.* **2008**, *155*, B897.
- [36] M. Wohlfahrt-Mehrens, J. Heitbaum, *J. Electroanal. Chem. Interfacial Electrochem.* **1987**, *237*, 251–260.
- [37] K. Macounova, M. Makarova, P. Krtil, *Electrochem. Commun.* **2009**, *11*, 1865–1868.
- [38] J. Rossmeisl, Z.-W. Qu, H. Zhu, G.-J. Kroes, N. J. K. Nørskov, *J. Electroanal. Chem.* **2007**, *607*, 83–89.
- [39] E. A. Paoli, F. Masini, R. Frydendal, D. Deiana, C. Schlaup, M. Malizia, T. W. Hansen, S. Horch, I. E. L. Stephens, I. Chorkendorff, *Chem. Sci.* **2015**, *6*, 190–196.
- [40] R. Frydendal, E. A. Paoli, I. Chorkendorff, J. Rossmeisl, I. E. L. Stephens, *Adv. Energy Mater.* **2015**, *7*, 1500991.
- [41] P. P. Patel, M. K. Datta, O. I. Velikokhatnyi, R. Kuruba, K. Damodaran, P. Jampani, B. Gattu, P. M. Shanthi, S. S. Damle, P. N. Kumta, *Sci. Rep.* **2016**, *6*, 28367.
- [42] N. Danilovic, R. Subbaraman, K. C. Chang, S. H. Chang, Y. J. Kang, J. Snyder, A. P. Paulikas, D. Strmcnik, Y. T. Kim, D. Myers, V. R. Stamenkovic, N. M. Markovic, *Angew. Chem. Int. Ed.* **2014**, *126*, 14240–14245.
- [43] N. Maheswari, G. Muralidharan, *Appl. Surf. Sci.* **2017**, *416*, 461–469.
- [44] J. Park, J. Joo, S. G. Kwon, Y. Jang, T. Hyeon, *Angew. Chem. Int. Ed.* **2007**, *46*, 4630–4660; *Angew. Chem.* **2007**, *119*, 4714–4745.
- [45] E. Budiyo, M. Yu, M. Chen, S. DeBeer, O. Rüdiger, H. Tüysüz, *ACS Appl. Energ. Mater.* **2020**, *3*, 8583–8594.
- [46] X. Deng, K. Chen, H. Tüysüz, *Chem. Mater.* **2017**, *29*, 40.

Manuscript received: October 13, 2021

Revised manuscript received: November 29, 2021

Accepted manuscript online: November 30, 2021

Version of record online: December 18, 2021